nature methods

BRIEF COMMUNICATION

https://doi.org/10.1038/s41592-018-0115-y

Three-photon imaging of mouse brain structure and function through the intact skull

Tianyu Wang[1*], Dimitre G. Ouzounov[1], Chunyan Wu[1], Nicholas G. Horton[1], Bin Zhang[2], Cheng-Hsun Wu[2], Yanping Zhang[2,3], Mark J. Schnitzer[2,3] and Chris Xu[1*]

Optical imaging through the intact mouse skull is challenging because of skull-induced aberrations and scattering. We found that three-photon excitation provided improved optical sectioning compared with that obtained with two-photon excitation, even when we used the same excitation wavelength and imaging system. Here we demonstrate three-photon imaging of vasculature through the adult mouse skull at >500-µm depth, as well as GCaMP6s calcium imaging over weeks in cortical layers 2/3 and 4 in awake mice, with 8.5 frames per second and a field of view spanning hundreds of micrometers.

Observation of the mouse brain in its native environment is critical to the study of neural network function and disease progression[1]. Cranial-window implantation[2] and skull thinning[3,4] are minimally invasive procedures that are commonly used to obtain optical access to the mouse brain; however, they can cause perturbation to the physiological environment. For example, mechanical stress during surgery can induce the activation of microglia and astrocytes[3,5], and skull openings can potentially change intracranial pressure and affect fluid flow in the paravascular space, which may be important for waste disposal[6]. Therefore, improved options for imaging through the intact skull would create new opportunities in noninvasive brain research.

Non-fluorescence-based technologies such as magnetic resonance imaging[7], photoacoustic tomography[8], and optical microangiography[9] can be used to map brain structure and hemodynamics through the intact skull. However, these technologies typically cannot achieve single-cell or subcellular resolution, and none of them is established for direct cellular activity measurement with high temporal resolution (for example, >1 Hz).

One-photon fluorescence, in combination with either infrared dyes[10] or skull-clearing techniques[11,12], can be used to image vasculature and neuronal activity through the skull. However, such methods generally do not offer single-cell resolution, because of out-of-focus fluorescence excitation.

Two-photon microscopy (2PM) is routinely used for in vivo deep brain imaging because of its optical-sectioning capability in scattering media[13]; however, 2PM yields poor resolution when used to image through an intact skull[14]. Although wavefront correction enabled 2PM to achieve submicrometer resolution, the corrected field of view (FOV) was about 23 × 23 µm, and the imaging depth was limited to approximately 50 µm in the cortex[14]. Recently, chemical treatment of the skull surface has been applied to improve the contrast of structural 2PM in shallow cortex[15,16].

Three-photon microscopy (3PM) increases the achievable imaging depth in mouse brain because it results in weaker scattering at longer excitation wavelengths and background suppression by higher-order nonlinear excitation, and 3PM imaging studies have revealed structure and function in the mouse hippocampus through cranial windows in intact brains[17,18]. Recently, vasculature imaging through intact mouse skull with a synthesized dye of unusually large three-photon excitation (3PE) cross-section at 1,550 nm reached a depth of 300 µm[19]. Here we show that 3PM not only achieves a cortical depth of more than 500 µm with conventional dyes but also is capable of calcium-activity imaging at high spatial and temporal resolution with FOVs of hundreds of micrometers.

The refractive index of cranial bone (~1.55) is substantially higher[20] than that of water (1.32) or cerebrospinal fluid (~1.34)[21]. This high refractive index and the rough surface of the skull, especially after exposure to air[11], render the skull opaque by scattering light like optical diffusers do. We found that we could reduce skull surface roughness by using an index-matching glue, which also insulated the skull from the air and preserved transparency for chronic imaging (Fig. 1a, Supplementary Fig. 1). After the treatment, we measured the effective attenuation length[17] (l_e) of the skull by using the third harmonic generation (THG) signal from osteocytes, and we found $l_e \sim 60$ µm at 1,320 nm (Fig. 1).

We compared 2PM at 920 nm and 3PM at 1,320 nm by imaging fluorescein-labeled vasculature in the same mouse through the intact skull around the center of the parietal bone. We observed that 1,320-nm 3PM resolved capillary vessels with high contrast (Fig. 1b, Supplementary Fig. 2a), with a signal-to-background ratio (SBR) close to 100 at 120-µm cortical depth and ~10 at 510-µm depth (Fig. 1c). In comparison, 920-nm 2PM had substantially lower contrast, with background tens of times higher in the unlabeled region of the brain even at shallow depths (Fig. 1c). We verified that 920-nm 2PM generated negligible intrinsic autofluorescence in the emission band of fluorescein by imaging the mouse before any dye injection. Therefore, the background in 2PM is fluorescence from fluorescein.

To delineate the effects of a longer wavelength and the higher-order nonlinear excitation in through-skull imaging, we injected Alexa Fluor 680 into a mouse that had previously been injected with fluorescein, and immediately carried out two-photon excitation (2PE) imaging of Alexa Fluor 680 at 1,320 nm with the same laser and microscope used for fluorescein imaging. The 1,320-nm 2PM had a similar SBR as 920-nm 2PM at all depths, with only limited improvement in contrast, presumably due to the reduced scattering and aberration at the longer excitation wavelength (Fig. 1b–d; the background was also verified as fluorescence from Alexa Fluor 680). These results show that a longer excitation wavelength alone is not sufficient, and 3PE is necessary for through-skull imaging.

With cranial windows, the SBR of 2PM remains high until the imaging depth is greater than ~4 scattering lengths[13]. However,

[1]School of Applied and Engineering Physics, Cornell University, Ithaca, NY, USA. [2]CNC Program, Stanford University, Stanford, CA, USA. [3]Howard Hughes Medical Institute, Stanford University, Stanford, CA, USA. *e-mail: tw329@cornell.edu; cx10@cornell.edu

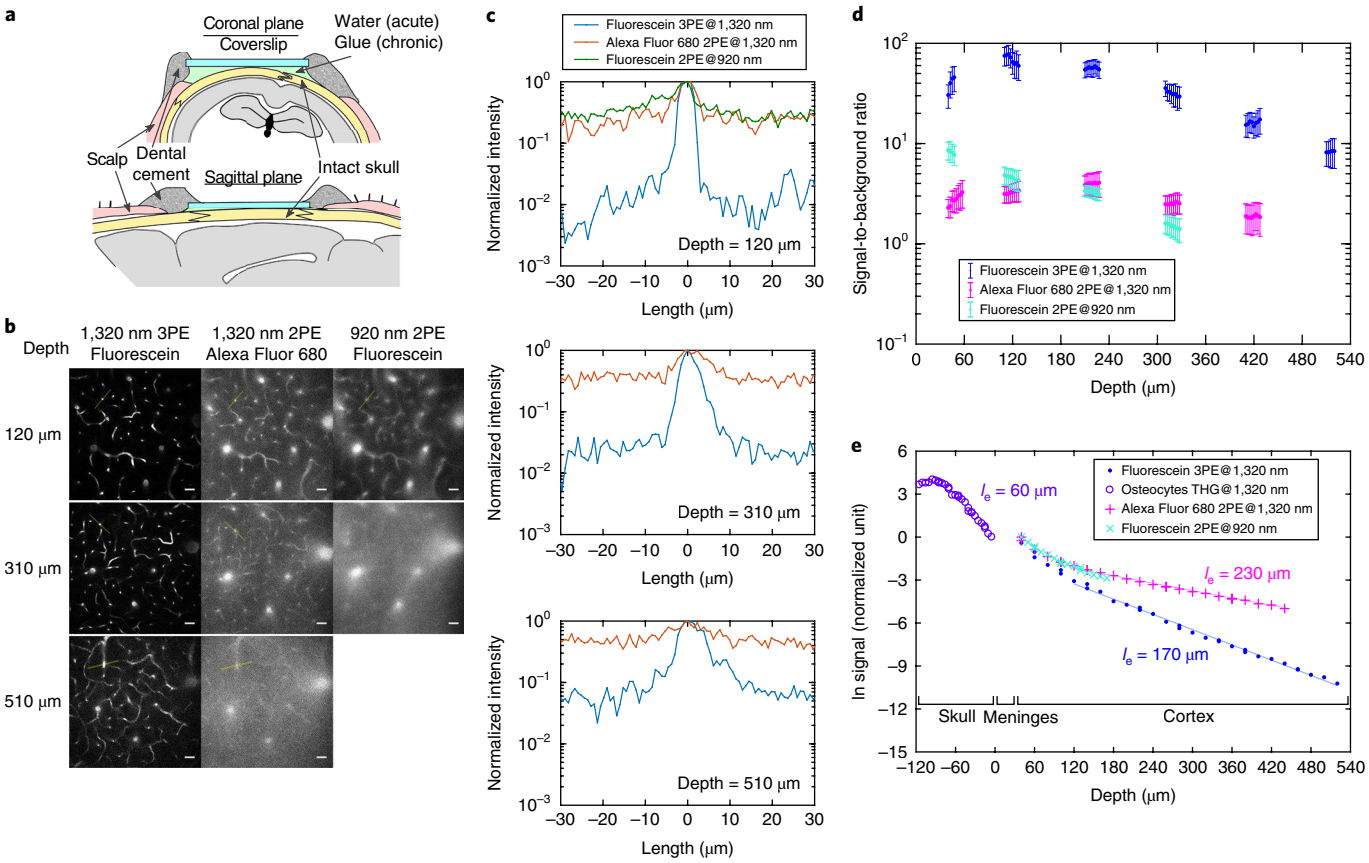

Fig. 1 | Comparison of through-skull vasculature imaging by 3PM and 2PM. a, Schematic of through-skull imaging preparation, showing coronal and sagittal views (see also Supplementary Fig. 1). **b**, Comparison of 2PM and 3PM images of the vasculature in a wild-type mouse (C57BL/6J, male, 12 weeks old; similar results for $n = 3$) acquired in the same cortical column under the central area of a parietal bone, with chronic preparation. Each site was imaged by 920-nm 2PE of fluorescein, 1,320-nm 3PE of fluorescein, and 1,320-nm 2PE of Alexa Fluor 680 during the same imaging session. For 920-nm 2PE, no image is shown for the 510-μm depth because the maximum imaging depth achieved was 420 μm (Supplementary Fig. 2). Each frame was integrated for 50 s to ensure that photon shot noise was negligible, and all image contrasts were linearly stretched to saturate the top 0.2% of pixels. Scale bars, 30 μm. **c**, Intensity profiles across the brightest blood vessels from each frame in **b** (that is, along the yellow lines in **b**; similar results for $n = 3$). **d**, SBR measured at different depths for the three imaging groups in **b** (similar results for $n = 2$). The signal was calculated from the average of the top 0.1% brightest pixels in each frame and background from the average of the unlabeled regions. Each data point was calculated from one image; vertical error bars indicate the s.d. of the SBR, originating from the variation in brightness of blood vessels in each image. **e**, Signal attenuation with depth for through-skull vasculature imaging measured in the same mouse as in **b** (similar results for $n = 2$). Meninges included dura mater, arachnoid, and pia mater. The signal strength at a particular depth is represented by the average value of the brightest 0.5% of the pixels in the x–y image from that depth. The effective attenuation length l_e was determined by exponential fit of the signal as a function of imaging depth (THG signal was used inside the skull). Each data point was calculated from one image.

in our through-skull experiment, the SBR of 2PM, even with 1,320-nm excitation, was less than 10 immediately beneath the skull (Fig. 1c,d). The skull accounts for approximately 2 attenuation lengths, and has low labeling density owing to the sparsity of vasculature in the bone. Therefore, the background in 2PM must be caused by the degradation of the point spread function (PSF) in both lateral (xy) and axial (z) dimensions. For example, in our study, the lateral broadening of the PSF was indicated by the blurred edges of capillaries in 2PM images (Fig. 1b); the axial elongation was indicated by the observation that large, penetrating blood vessels were much brighter than horizontal capillaries in 2PM compared with 3PM (Fig. 1b). The higher-order nonlinear excitation of 3PM was more effective in accentuating the central peak (that is, the signal) and suppressing the unwanted fluorescence excitation from the side lobes (that is, the background) of the PSF. Therefore, 3PE helps to preserve spatial resolution and improve image contrast when the presence of the intact skull degrades the PSF. This explanation is further corroborated by the measured attenuation length of the brain tissue for through-skull imaging, which was shorter in 3PM than in 2PM (Fig. 1e, Supplementary Note 1).

To provide an upper-bound estimate of the spatial resolution of through-skull imaging, we measured the fluorescence intensity profile of a dendrite (Fig. 2a–d). The lateral and axial FWHM was 0.96 μm and 4.6 μm, respectively, which provided the upper bound of the spatial resolution owing to the finite size of the neural processes. 2PM at 920 nm could not resolve any feature at high spatial resolution in the same GCaMP6s mice (Supplementary Fig. 2b).

We imaged spontaneous activities of GCaMP6s-labeled neurons in adult transgenic mice (*CamKII-tTA/tetO-GCaMP6s*, 8–12 weeks old (both male and female mice used), $N = 5$). Figure 2e shows an imaging site in cortical layer 2/3 of an 8-week-old mouse with an ~120-μm-thick skull. We recorded neuronal activity traces under awake conditions (Fig. 2f). We ascertained the absolute signal-to-noise ratio (SNR) of the recording from the raw photon counts (Supplementary Fig. 3), which is comparable to the procedure for typical 2PM calcium imaging through a cranial window. As imaging

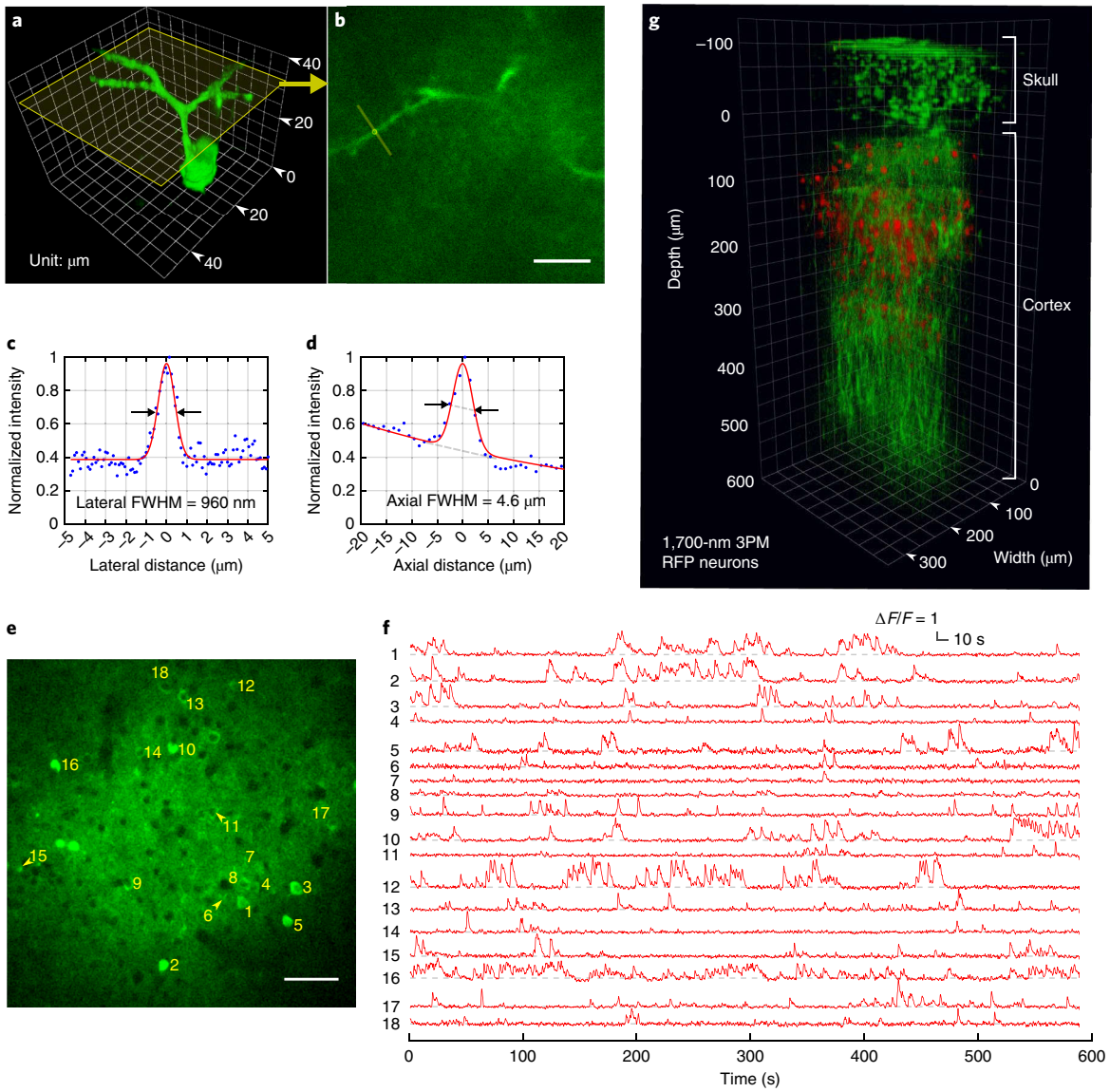

Fig. 2 | Through-skull imaging of neural structure and function. a, 3D reconstruction of a GCaMP6s-labeled neuron located about 140 μm below the cortical surface in a transgenic mouse imaged by 1,320-nm 3PM through an intact skull of ~100-μm thickenss (*CamKII-tTA/tetO-GCaMP6s* mouse, 10 weeks old; similar measurements were performed on 3 neurons in each of 2 mice, for a total $n=6$). **b**, A cross-section of the 3D stack along the yellow frame in **a**. Measurements for lateral and axial resolution on the apical dendrite were taken at the locations indicated by the yellow line and circle, respectively (similar results for $n=6$). Scale bar, 10 μm. **c**, Lateral intensity profile measured along the yellow line in **b**, fitted by a Gaussian profile for the estimation of the lateral resolution (similar results for $n=6$). **d**, Axial intensity profile measured in the region within the yellow circle in **b**, fitted by the sum of two Gaussian profiles, with one broad, off-centered Gaussian profile to correct for the uneven baseline, and the other for the central peak (similar results for $n=6$). **e**, High-resolution image of a site for through-skull activity recording in an awake, GCaMP6s-labeled transgenic mouse (*CamKII-tTA/tetO-GCaMP6s*, female, 8 weeks old; similar results for $n=5$). The recording site was about 275 μm below the cortical surface, and the FOV was 320 μm × 320 μm (256 × 256 pixels per frame). Scale bar, 50 μm. **f**, Spontaneous activity traces recorded under awake conditions from the indexed neurons in **e**, acquired at a frame rate of 8.49 Hz (similar results for $n=5$). The repetition rate used for imaging was 800 kHz, and the average power under the objective lens was 44 mW. Each trace was normalized to its baseline and low-pass filtered by a hamming window of 1.06-s time constant. The same site was visited eight times over a period of 4 weeks after the skull preparation, with a cumulative total of over 6 h of recording time (data from other imaging sessions are shown in Supplementary Fig. 5). **g**, 3D reconstruction of through-skull imaging of a cortical column of red fluorescent protein (RFP)-labeled neurons in a Brainbow mouse (B6.Cg-Tg(Thy1-Brainbow1.0)HLich/J, male, 12 weeks old; similar results for $n=2$). The red channel is the 3PE fluorescent signal from RFP, and the green channel is THG. The zero depth is set just beneath the skull.

depth increased, the $\Delta F/F$ value (where F is the fluorescence intensity) for through-skull 3PM decreased because of the increased background contribution (Fig. 1e). To maintain the SNR and temporal resolution, we had to increase the photon counts per neuron per second by either delivering additional power to the focus or reducing the FOV. The deepest activity imaging in this study was at 465 μm below the cortical surface (Supplementary Fig. 4). Although through-skull 3PM provided sufficient SNR to record activity with GCaMP6s in cortical layer 2/3 neurons, it required a higher average and peak power than 2PM with cranial windows because of the combined effects of skull attenuation and inefficient higher-order nonlinear excitation. These power requirements ultimately limited

the performance of through-skull 3PM (Supplementary Note 2). Therefore, 2PM imaging through cranial windows remains the preferred method if the experimental results are not expected to be affected by the craniotomy.

We performed a longitudinal study and recorded from the same neurons on 8 different days over a period of 4 weeks after the initial skull preparation (Supplementary Figs. 4a and 5 show longitudinal recordings from three sites at different depths). We used the THG signal from the blood vessels to locate approximately the same imaging FOV for each recording session. Despite the long exposure time (a cumulative total of more than 6 h per recording site), we did not observe visible adverse effects on neuronal structure or activity, which indicated that the average power and the peak intensity were safe for imaging. We also carried out immunostaining of the brains after imaging and confirmed that there was no measurable tissue damage under the imaging conditions used for activity recording in this study (Supplementary Fig. 6). We observed some degradation of skull transparency over time, as indicated by the power needed to image the same site in repeated sessions (for example, 35–50% more power after 4 weeks; Supplementary Fig. 5). Nonetheless, we were able to obtain successful recordings of neuronal activity in all imaging sessions.

In addition to 1,320-nm 3PM, we tested 1,700-nm 3PM for through-skull structural imaging of Texas Red–labeled vasculature and red-fluorescent-protein-labeled neurons, and were able to image successfully at cortical depths of more than 500 µm with both (Fig. 2g, Supplementary Fig. 7).

We have demonstrated through-skull 3PM of mouse brain structure and function, with high spatial and temporal resolution and large FOVs, and at substantial depth. Furthermore, by comparing 2PM and 3PM at the same excitation wavelength, we determined that 3PE is necessary for imaging through intact skull, regardless of the imaging depth and the labeling density. This work demonstrates the advantage of higher-order nonlinear excitation for imaging through a highly scattering layer, which is in addition to the previously reported advantage of 3PM for deep imaging of densely labeled samples. The demonstrated technique will lead to new opportunities for noninvasive studies of live biological systems.

Online content

Any methods, additional references, Nature Research reporting summaries, source data, statements of data availability and associated accession codes are available at https://doi.org/10.1038/s41592-018-0115-y.

Received: 28 January 2018; Accepted: 26 June 2018;
Published online: 10 September 2018

References

1. McGonigle, P. *Biochem. Pharmacol.* **87**, 140–149 (2014).
2. Holtmaat, A. et al. *Nat. Protoc.* **4**, 1128–1144 (2009).
3. Yang, G., Pan, F., Parkhurst, C. N., Grutzendler, J. & Gan, W.-B. *Nat. Protoc.* **5**, 201–208 (2010).
4. Drew, P. J. et al. *Nat. Methods* **7**, 981–984 (2010).
5. Dorand, R. D., Barkauskas, D. S., Evans, T. A., Petrosiute, A. & Huang, A. Y. *Intravital* **3**, e29728 (2014).
6. Rangroo Thrane, V. et al. *Sci. Rep.* **3**, 2582 (2013).
7. Jonckers, E., Shah, D., Hamaide, J., Verhoye, M. & Van der Linden, A. *Front. Pharmacol.* **6**, 231 (2015).
8. Wang, X., Pang, Y., Ku, G., Stoica, G. & Wang, L. V. *Opt. Lett.* **28**, 1739–1741 (2003).
9. Wang, R. K. et al. *Opt. Express* **15**, 4083–4097 (2007).
10. Hong, G. et al. *Nat. Photonics* **8**, 723–730 (2014).
11. Silasi, G., Xiao, D., Vanni, M. P., Chen, A. C. N. & Murphy, T. H. *J. Neurosci. Methods* **267**, 141–149 (2016).
12. Steinzeig, A., Molotkov, D. & Castrén, E. *PLoS One* **12**, e0181788 (2017).
13. Theer, P. & Denk, W. *J. Opt. Soc. Am. A. Opt. Image. Sci. Vis.* **23**, 3139–3149 (2006).
14. Park, J.-H., Sun, W. & Cui, M. *Proc. Natl Acad. Sci. USA* **112**, 9236–9241 (2015).
15. Zhao, Y.-J. et al. *Light Sci. Appl.* **7**, 17153 (2018).
16. Zhang, C. et al. *Theranostics* **8**, 2696–2708 (2018).
17. Horton, N. G. et al. *Nat. Photonics* **7**, 205–209 (2013).
18. Ouzounov, D. G. et al. *Nat. Methods* **14**, 388–390 (2017).
19. Wang, Y. et al. *ACS Nano* **11**, 10452–10461 (2017).
20. Ascenzi, A. & Fabry, C. *J. Biophys. Biochem. Cytol.* **6**, 139–142 (1959).
21. Tuchin, V. V. *Tissue Optics: Light Scattering Methods and Instruments for Medical Diagnosis* 2nd ed. 143–256 (SPIE, Bellingham, WA, 2000).

Acknowledgements

We thank members of the Xu group and Schnitzer lab for discussion. We thank K. Podgorski and A. Hu (Janelia Research Campus) for advice on tissue-damage assessment. We also thank H.G. Chae and D. Florin Albeanu (Cold Spring Harbor Laboratory) for sharing the head-bar and holder design for awake imaging. Last, we thank the Warden lab (Cornell University) for providing the microtome for brain sectioning. The project was supported by DARPA (W911NF-14-1-0012 to C.X.; HR0011-16-2-0017 to M.J.S.), NIH/NINDS (U01NS090530 to C.X.), the National Science Foundation (NeuroNex Grant DBI-1707312 to C.X.), and the Intelligence Advanced Research Projects Activity (IARPA) via Department of Interior/Interior Business Center (DoI/IBC) (contract number D16PC00003 to C.X.). The US Government is authorized to reproduce and distribute reprints for Governmental purposes notwithstanding any copyright annotation thereon. Disclaimer: The views and conclusions contained herein are those of the authors and should not be interpreted as necessarily representing the official policies or endorsements, either expressed or implied, of IARPA, DoI/IBC, or the US Government.

Author contributions

C.X. conceived the study and supervised the project. T.W., D.G.O., and N.G.H. designed and performed the experiments. C.W. set up awake imaging and performed immunohistology. C.-H.W., B.Z., and Y.Z. tested skull preparations for improving the optical transparency of the cranium for long-term imaging. C.X. and M.J.S. supervised the study. T.W. analyzed the data. T.W. and C.X. prepared the manuscript.

Competing interests

The authors declare no competing interests.

Additional information

Supplementary information is available for this paper at https://doi.org/10.1038/s41592-018-0115-y.

Reprints and permissions information is available at www.nature.com/reprints.

Correspondence and requests for materials should be addressed to T.W. or C.X.

Publisher's note: Springer Nature remains neutral with regard to jurisdictional claims in published maps and institutional affiliations.

Methods

Experimental setup. The laser and microscope setup was similar to that in our previous work[18]. Any difference in system parameters is stated in this section.

Excitation source. The excitation source for 1,320-nm 3PM was a noncollinear optical parametric amplifier (NOPA; Spectra Physics) pumped by a regenerative amplifier (Spirit, Spectra Physics). We used a two-prism (SF11 glass) compressor to compensate for the normal dispersion of the optics of the light source and the microscope, including the objective lens. The NOPA operates at a wavelength centered at 1,320 nm and provides an average power of ~700 mW (1,750 nJ per pulse at a 400-kHz repetition rate). The pulse duration (measured by second-order interferometric autocorrelation) under the objective was ~37 fs after optimization of the prism compressor. An optical delayed line was used to double the laser repetition rate to 800 kHz by splitting the excitation beam into two equal powers and introducing an ~10-ns delay between their pulse trains.

The excitation source for 2PM was a mode-locked Ti:sapphire laser (Tsunami, Spectra Physics) centered at 920 nm. The 920-nm beam and 1,320-nm beam were spatially overlapped and directed to the same microscope, and then combined by a dichroic mirror.

The excitation source for 1,700-nm 3PM was solitons centered at 1,700 nm generated by soliton self-frequency shift in a photonic crystal fiber pumped by a fiber laser at 1,550 nm (described in more detail in ref. [22]).

Imaging setup. The images were acquired with a custom-built multiphoton microscope with a high-numerical-aperture objective (Olympus XLPLN25XWMP2; 25×/1.05-NA). The objective was under-filled to reduce unnecessary loss of power in the marginal rays, and the $1/e^2$ beam diameter of the excitation beam was ~11 mm, which is ~70% of the objective back aperture diameter.

The signal was epi-collected through the objective and then reflected by a dichroic beam splitter (FF705-Di01-25×36, Semrock) to the detection system. There were two detection channels: one for fluorescence signal and the other for THG. For GCaMP6s imaging, we used a photomultiplier tube (PMT) with a GaAsP photocathode (H7422-40, Hamamatsu) for the fluorescent signal and an ultra bialkali PMT (R7600-200, Hamamatsu) for the THG signal. A 488-nm dichroic beam splitter (Di02-R488-25×36, Semrock) was inserted at 45° to the signal beam path to separate and direct fluorescence and THG to their respective PMTs. Fluorescence generated by fluorescein and GCaMP6s was selected by a (520±30)-nm band-pass filter (Semrock), and THG around 440 nm was selected by a (435±20)-nm filter (Semrock). For Alexa Fluor 680 imaging, we switched to a GaAs PMT (H7422-50, Hamamatsu) for the fluorescence channel, because it had higher sensitivity at longer wavelengths. The fluorescence filter was also changed to a (716±20)-nm (Semrock) filter to pass Alexa Fluor 680 fluorescence while blocking the second harmonic of 1,320 nm.

For signal sampling, the PMT current was converted to voltage by a transimpedance amplifier with a 10-MHz bandwidth (C9999, Hamamatsu), which provided adequate temporal resolution for photon counting. For analog signal acquisition, an additional 1.9-MHz low-pass filter (Minicircuts, BLP-1.9+) was used before digital sampling. Analog-to-digital conversion was done by a data acquisition card (NI PCI-6115, National Instruments). The signal acquisition system displayed shot-noise-limited performance, and light shielding was carefully done to achieve dark counts of 20–40 photons per second under actual imaging conditions without laser scanning. ScanImage 3.8 running on MATLAB (MathWorks) was used to acquire images and control a 3D translation stage to move the sample (M-285, Sutter Instrument Company). All imaging depths and thicknesses are reported in raw axial movement of the motorized stage, unless otherwise stated. The refractive indices of skull and brain tissue (1.55 for the bone and 1.35–1.37 for the cortex[21]) are higher than that of water (1.32), which resulted in slight underestimation of the actual depth in the experiments (~12% for the skull thickness and ~3% for the depth in the brain tissue).

High-resolution structural images were typically taken with 512×512 pixels per frame, a 0.5-Hz frame rate, and multiple frame averages at each depth. Neuronal activities were recorded using 256×256 pixels per frame at an 8.49-Hz frame rate. Each site was recorded for 30–50 min in each imaging session. The conversion from pixel values to photon counts was done according to a previously described method[18].

For in vivo imaging, the mouse was placed on a tip-tilt stage under the objective lens. With this setup it is important to ensure that the skull surface and the coverslip are parallel to the imaging plane of the objective. In most cases, the skull is curved, and so it is preferable to adjust the tilt angle so that the apex of the curvature is directly above the imaging site.

Resolution measurement on dendrites. To eliminate the fluctuation in brightness caused by a changing calcium concentration, we intentionally damaged a neuron by continuous laser scanning for 4 min at high intensity (~9 nJ at the focus) and with a small FOV (20×20 µm). The damaged neuron had a constant GCaMP6s-fluorescence brightness. We then acquired a *z*-stack around the soma and its apical dendrites at 0.2-µm steps. We plotted intensity profiles of the dendrite either laterally or axially to estimate the resolution.

Image processing for activity recording. Mechanical drift in the horizontal plane, if present, was corrected by the TurboReg plug-in in ImageJ. Regions of interest were generated by manual segmentation of neuron bodies. In MATLAB, fluorescence intensity traces were low-pass filtered with a hamming window of a time constant of 1.06 s. Spikes were inferred according to ref. [23], assuming shot-noise-limited detection. We then determined baselines of the traces (F_0) by excluding the spikes and their rising and falling edges. Traces (F) were normalized according to the formula $(F - F_0)/F_0$. Examples of the raw-activity-recording videos played at a recording frame rate of 8.49 Hz with 2 frames rolling average are presented in Supplementary Video 1. For visual representation of calcium activities in Supplementary Video 2, the raw image sequence was first rolling-averaged with 17 frames, and then the local background was subtracted to improve contrast (ImageJ). The activity movie was further processed by Kalman filter with a gain from 0.7 to 0.9 for noise reduction[24] (ImageJ).

Image processing for structural imaging. Structural images were processed with a median filter of 1-pixel radius and then normalized by linear transform of pixel intensities to saturate the brightest 0.2–0.5% of pixels in each frame. Three-dimensional reconstruction of the stacks was rendered in Volocity (version 6.3). For the purpose of visualization, some of the high-resolution images in Fig. 2e and Supplementary Figs. 4 and 5 are displayed with a gamma correction value of 0.8–0.95 to reduce brightness contrast between different neurons.

Statistics and data analysis. All data analysis was performed in MATLAB 2016. The effective attenuation length in Fig. 1e was derived by least-squares linear regression of fluorescent signal data. For all representative results, the number of successful independent experiments on different animals is indicated in the corresponding figure legend, and more details on the ages of the animals are included in the Nature Research Reporting Summary.

Animal procedures. All animal experimentation and housing procedures were conducted in accordance with Cornell University Institutional Animal Care and Use Committee guidance.

Skull preparation for chronic imaging. Before the surgery, animals were anesthetized with isoflurane (3% in oxygen for induction, and 1.5–2% for surgery to maintain a breathing frequency around 1 Hz). Body temperature was kept at 37.5 °C with a feedback-controlled blanket (Harvard Apparatus), and eyes were covered with eye ointment. Glycopyrrolate (0.01 mg/kg body weight), dexamethasone (0.2 mg/kg body weight), and ketoprofen (5 mg/kg body weight) were administrated intramuscularly. Dexamethasone and ketoprofen were also administrated on the two consecutive days after the surgery. The anesthetized animal was fixed on a stereotaxic mount, and hair was removed from its scalp with scissors and Nair. The scalp was further sterilized with alcohol wipes, and then a section of scalp was removed to expose both parietal plates and the bregma and lambda. Sterile saline was applied to the skull immediately after the exposure, as it is critical to keep the entire bone surface covered by saline to insulate it from air. Fascia and connective tissue on the skull were gently removed with forceps and sterile wet cotton tips to avoid any internal bleeding inside the brain. At this point, the whole skull was transparent, with blood vessels underneath visible with sharp edges. The saline covering the skull was then wiped completely away with cotton tips, and the following actions were taken quickly before the bone turned opaque. Ultraviolet-curable glue (Loctite 4305) was applied to the skull surface within 2 s. A sterile and dry round coverslip of 5-mm diameter (#1 thickness; Electron Microscopy Sciences) was placed on the skull, centered at 2.5 mm lateral and 2 mm caudal from the bregma point. The coverslip was pressed closely against the skull surface with forceps to minimize the amount of glue between the coverslip and the skull. The glue was left to cure by itself for about 5 min without any ultraviolet light, during which time the skull transparency tended to increase visually. Afterward, an ultraviolet light source (385–515 nm; Bluephase Style 20i, Ivoclar vivadent) was used to completely cure the glue, with roughly 1 s on and 1 s off for 3 s. The coverslip was necessary to keep the glue layer as thin as possible (down to ~10 µm at the thinnest part on the skull) and to form a flat interface to reduce aberration. The exposed part of the skull surrounding the coverslip was further covered with dental cement. Supplementary Fig. 1 shows an example of a successful preparation. For awake imaging, a head bar for head fixation during imaging was glued to the exposed parts of the skull surrounding the coverslip with metabond glue.

Imaging procedures. For imaging of anesthetized animals, the mice were anesthetized with isoflurane (1–1.5% in oxygen, with breathing frequency maintained at 2 Hz) and placed on a heat blanket to maintain body temperature at 37.5 °C. Eye ointment was applied and the animal was placed on a 3D motorized stage for navigation under the microscope. For structural imaging, the vasculature of wild-type mice ($N = 3$, 10–12 weeks old, male, C57BL/6J, The Jackson Laboratories) was labeled via retro-orbital injection of fluorescein, Alexa Fluor 680,

and Texas Red (25 mg of dextran conjugate dissolved in 200 µl of sterile saline, 10-kDa molecular weight; Invitrogen).

For awake imaging, we fixed the animal on a custom-made stereotaxic plate by attaching its head-bar to the metal holders. The body of the animal was further secured in a tube of slippery inner walls to reduce motion.

Immunohistochemistry for tissue damage assessment. Anesthetized mice were continuously imaged with 1,320-nm 3PM with the laser operating at a 400-kHz repetition rate. The scanned region was ~2.5 mm lateral and 1 mm caudal to the bregma point. A 200 × 200 µm FOV at ~200-µm cortical depth was continuously scanned for 30 min, at 60 mW average power under the objective lens for one mouse and at 120 mW for the other. After 16 h, mice were transcardially perfused, and the brains were postfixed. The brain fixation and antibody staining procedures followed a previously described protocol[23] (detailed information on the antibodies used in this study is included in the Nature Research Reporting Summary). Coronal sections were cut in 50-µm-thickness steps through the center of the imaged region, and alternating slices were labeled for heat shock protein (HSP) and glial fibrillary acidic protein (GFAP). The brain slices were imaged with a Zeiss 780 confocal microscope.

Reporting Summary. Further information on research design is available in the Nature Research Reporting Summary linked to this article.

Data availability

The data that support the findings of this study are available from the corresponding author upon request.

References

22. Horton, N. G. & Xu, C. *Biomed. Opt. Express* **6**, 1392–1397 (2015).
23. Podgorski, K. & Ranganathan, G. *bioRxiv* Preprint at https://www.biorxiv.org/content/early/2016/06/06/057364 (2016).
24. Yuryev, M. et al. *Front. Cell. Neurosci.* **9**, 500 (2016).

nature research

Corresponding author(s): Tianyu Wang

Life Sciences Reporting Summary

Nature Research wishes to improve the reproducibility of the work that we publish. This form is intended for publication with all accepted life science papers and provides structure for consistency and transparency in reporting. Every life science submission will use this form; some list items might not apply to an individual manuscript, but all fields must be completed for clarity.

For further information on the points included in this form, see Reporting Life Sciences Research. For further information on Nature Research policies, including our data availability policy, see Authors & Referees and the Editorial Policy Checklist.

Please do not complete any field with "not applicable" or n/a. Refer to the help text for what text to use if an item is not relevant to your study.
For final submission: please carefully check your responses for accuracy; you will not be able to make changes later.

Experimental design

1. Sample size

   Describe how sample size was determined.

   Most of our conclusions do not rely on sample size, either because there is essentially zero overlapping in statistical distribution of the parameters to be compared (e.g. orders of magnitude difference in signal-to-background ratio), or the measurement inherently integrates multiple measurements (e.g. using regression to calculate attenuation lengths, structural imaging with multiple averages at the same site). We typically repeat the imaging experiment on 3 animals to ensure similar results are reproducible.

2. Data exclusions

   Describe any data exclusions.

   We only excluded data whose quality was compromised by identifiable reasons, such as flawed surgical operation, GCaMP6 expression failure, and inactivity due to the random nature of spontaneous activity.

3. Replication

   Describe the measures taken to verify the reproducibility of the experimental findings.

   We performed identical independent experiments on different animals of similar age to ensure the results are reproducible. Every replicate for vascular or neuronal structure imaging was successful (n=3 for 1320-nm 3PM vasculature imaging; n=2 for 1700-nm 3PM RFP neurons; n=2 for GCaMP6 dendritic resolution measurement). For calcium imaging in cortical layer 2/3, every replicate with good surgery and <= 120 um skull thickness produced similar results as in the paper (n=5).

4. Randomization

   Describe how samples/organisms/participants were allocated into experimental groups.

   No group was allocated in this study, and any experiment involving comparison of imaging methods was done on the same animal during the same imaging session.

5. Blinding

   Describe whether the investigators were blinded to group allocation during data collection and/or analysis.

   Not applicable, since no group was allocated.

Note: all in vivo studies must report how sample size was determined and whether blinding and randomization were used.

6. Statistical parameters

For all figures and tables that use statistical methods, confirm that the following items are present in relevant figure legends (or in the Methods section if additional space is needed).

n/a	Confirmed
☐	☒ The exact sample size (*n*) for each experimental group/condition, given as a discrete number and unit of measurement (animals, litters, cultures, etc.)
☐	☒ A description of how samples were collected, noting whether measurements were taken from distinct samples or whether the same sample was measured repeatedly
☐	☒ A statement indicating how many times each experiment was replicated
☒	☐ The statistical test(s) used and whether they are one- or two-sided *Only common tests should be described solely by name; describe more complex techniques in the Methods section.*
☒	☐ A description of any assumptions or corrections, such as an adjustment for multiple comparisons
☒	☐ Test values indicating whether an effect is present *Provide confidence intervals or give results of significance tests (e.g. P values) as exact values whenever appropriate and with effect sizes noted.*
☒	☐ A clear description of statistics including central tendency (e.g. median, mean) and variation (e.g. standard deviation, interquartile range)
☐	☒ Clearly defined error bars in all relevant figure captions (with explicit mention of central tendency and variation)

See the web collection on statistics for biologists for further resources and guidance.

Software

Policy information about availability of computer code

7. Software

Describe the software used to analyze the data in this study.

FIJI ImageJ was used for interactive image operation, including motion correction with TurboReg plugin, manual cell body segmentation, selecting gamma value for display purpose only (no quantitative information was drawn from any image after gamma correction), Kalman filter setting for activity visualization in supplementary video 1.

MATLAB 2016B was used for basic batch image operation (e.g. background subtraction, averaging, linear contrast stretch); processing of activity traces exported from ImageJ (e.g. low-pass filtering, background determination, and normalization).

Volocity was used for 3D rendering of structural stacks.
ffmpeg was used for video compression and encoding.

For manuscripts utilizing custom algorithms or software that are central to the paper but not yet described in the published literature, software must be made available to editors and reviewers upon request. We strongly encourage code deposition in a community repository (e.g. GitHub). *Nature Methods* guidance for providing algorithms and software for publication provides further information on this topic.

Materials and reagents

Policy information about availability of materials

8. Materials availability

Indicate whether there are restrictions on availability of unique materials or if these materials are only available for distribution by a third party.

All experimental materials in this study are available from standard commercial sources.

9. Antibodies

Describe the antibodies used and how they were validated for use in the system under study (i.e. assay and species).

Primary antibodies used for immunohistochemistry were mouse monoclonal anti-GFAP (Sigma-Aldrich; Cat. #: G3893; Clone Name: G-A-5, Mouse Ascites Fluid; Lot. #: 107M4792V; 1:1,000 dilution) and anti-HSP70/HSP72 (C92F3A-5) (Enzo; Cat. #: ADI-SPA-810-F; Clone Name: C92F3A-5; Lot #: 05021648; 1:400 dilution). The secondary antibodies used was Goat-anti-Mouse IgG Alexa Fluor 594 (invitrogen; Cat. #: A11032; Lot. #: 1922849; 1:500 dilution). We completely followed the protocol for biohistochemistry in ref. 24 at the end of "Online Method". The certificates of analysis of the antibodies can be found by searching Lot. numbers on their websites.

10. Eukaryotic cell lines

a. State the source of each eukaryotic cell line used.

No eukaryotic cell line was used in this study.

b. Describe the method of cell line authentication used.

No eukaryotic cell line was used in this study.

c. Report whether the cell lines were tested for mycoplasma contamination.

No eukaryotic cell line was used in this study.

d. If any of the cell lines used are listed in the database of commonly misidentified cell lines maintained by ICLAC, provide a scientific rationale for their use.

No eukaryotic cell line was used in this study.

Animals and human research participants

Policy information about studies involving animals; when reporting animal research, follow the ARRIVE guidelines

11. Description of research animals

Provide all relevant details on animals and/or animal-derived materials used in the study.

For 1320-nm 3PM vasculature imaging, we used wild-type mice (C57BL/6J; male; adult; the Jackson Laboratory; n=3, age=12,14, and 15 weeks old).
For 1700-nm 3PM neuronal structure imaging, we used Brainbow mice (B6.Cg-Tg(Thy1-Brainbow1.0)HLich/J; male; adult; the Jackson Laboratory; n=2, age=12 and 8 weeks old.).
For in vivo calcium imaging with GCaMP6s, we used transgenic mice crossed from Tg(tetO-GCaMP6s)2Niell/J (The Jackson Laborary) and CaMKII-tTA (The Jackson Laboratory). We imaged 4 females and 1 male. The mean age at the time of imaging was 10 weeks old, and the range was 8-12 weeks old.

Policy information about studies involving human research participants

12. Description of human research participants

Describe the covariate-relevant population characteristics of the human research participants.

This study did not involve any human participant.